ACS OMEGA

http://pubs.acs.org/journal/acsodf

Article

Room-Temperature Ferromagnetism in Mn-Doped ZnO Nanoparticles Synthesized by the Sol–Gel Method

Sidra Kanwal, Muhammad Tahir Khan,* Vineet Tirth, Ali Algahtani, Tawfiq Al-Mughanam, and Abid Zaman*

Cite This: *ACS Omega* 2023, 8, 28749–28757

Read Online

ACCESS | Metrics & More | Article Recommendations

ABSTRACT: In the current work, pure ZnO and Mn-doped ZnO nanoparticles were synthesized by the sol–gel autocombustion method. Structural analysis and phase determination were done by X-ray diffraction, and a hexagonal wurtzite structure was exhibited with disparate microstructures for all samples. Mn^{2+} ions were well composed, as evidenced by the fluctuation of lattice parameters, dislocation density, and lattice strain. Crystallite size decreases from 38.42 to 27.54 nm by increasing the doping concentration. Field emission scanning electron microscopy results shows the combination of evenly distributed spherical-like and hexagon-like structures. Fourier transform infrared spectra revealed that when Mn content increased, the absorption bands red-shifted. The drop in the energy band gap from 3.25 eV for ZnO to 2.99 eV for $Zn_{0.96}Mn_{0.04}O$ was predicted by ultraviolet–visible absorption spectra. This red shift in the energy band gap can be explained by the sp–d exchange interaction between the band electrons of ZnO and localized d electrons of Mn. A study of magnetic properties revealed the change of the diamagnetic attribute for pure ZnO to the room-temperature ferromagnetic attribute of doped samples. In the current study, room-temperature ferromagnetism was achieved for Mn-doped ZnO nanoparticles, which can serve as a desirable option for practical applications in the future.

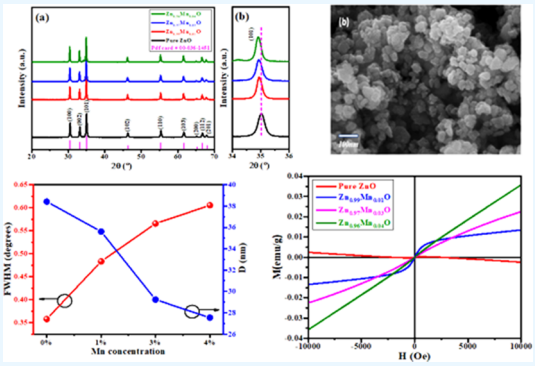

INTRODUCTION

Nanotechnology, which deals with particles of sizes in the range of 1–100 nm and have a high surface-to-volume ratio, is an expanding field in materials science. These particles exhibit greatly manageable physical, optical, structural, and magnetic properties depending upon their size.[1] Magnetic NPs are of great interest to investigators from a range of disciplines, which include heterogeneous and homogeneous catalysis, biomedicine, magnetic fluids, data storage magnetic resonance imaging (MRI), photocatalysis, photo optics, electronic devices, and environmental remediation such as water decontamination.[2,3] The literature revealed that NPs performed best when the size was in the range of 10–20 nm.[4] At such a low scale, the magnetic properties of NPs dominate effectively and they possess exceptional strength and toughness due to the effective regulatory mechanism and the electrostatic interactions, which make these particles priceless and they can be used in different applications.[5] Charge-based semiconductors and spin-based magnetism are connected via diluted magnetic semiconductors (DMSs). Spin addition to basic electronics increases their application hugely including faster operation, storage density, and reduction in the rate of energy consumption.[6,7] By using both the spin and charge of electrons, we will be able to use the ability to process information and mass storage in the same system. The lower solubility of magnetic elements in compounds makes it difficult to make semiconductors magnetic. The control of both spin and charge of electrons can be advantageous in semiconductors that have room-temperature ferromagnetism (RTFM).[8]

In order to achieve room-temperature ferromagnetism, the use of oxide-based semiconducting hosts is given preference because they have a wide band gap, i.e., clear to visible light, and can be densely doped with n-type carriers. Oxide-based semiconductors also have the capability to grow at low temperatures, which will help in restricting the sample to a single phase. Even if many NPs demonstrate their effectiveness in various technological domains, ZnO has taken the center stage because of its extensive applications in LEDs, solar cells, ultraviolet lasers, piezoelectric devices, transparent conducting oxide (TCO), etc.[9,10]

Received: May 21, 2023
Accepted: July 12, 2023
Published: July 26, 2023

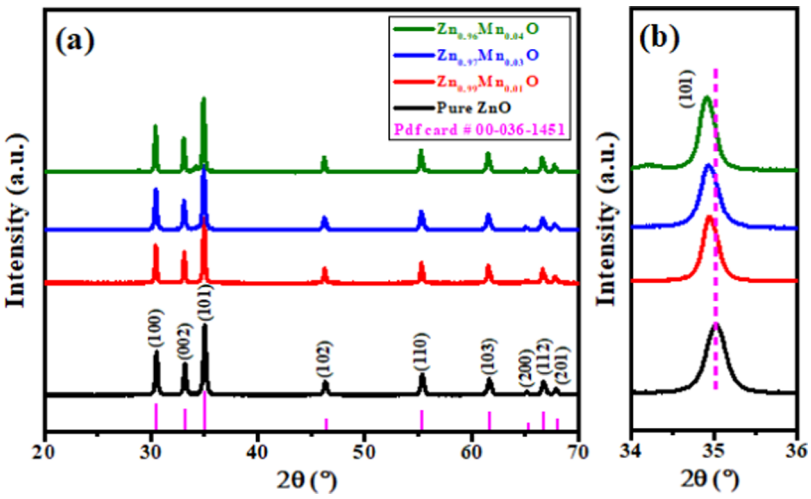

Figure 1. (a) XRD patterns of pure ZnO and Mn-doped ZnO nanoparticles. (b) Zoomed view of the peak of (1 0 1) shifting toward lower 2θ.

The interest in ZnO for the development of these DMSs developed from the theoretical work of Dietl et al.,[11] who produced a material with ferromagnetic behavior above room temperature using ZnO doped with 0.05 mol of Mn^{2+} with electrons or hole concentrations (3.5×10^{20} cm^{-3}). Dietl et al.'s studies inspired numerous subsequent studies of ZnO to obtain DMSs for spintronic applications.[12] ZnO is well known for unique characteristics like high electron mobility, a wide band gap of ~3.4 eV even at room temperature, and good transparency. Room-temperature ferromagnetism can be obtained by doping noble metals (Pd, Ag, Pt, etc.) or transition metals (Al, Cr, Mn, Fe, Ni, Cu, Co, etc.). Transition metal (TM)-doped ZnO nanoparticles are characterized by strong coupling between localized d electrons of the TM ions and the extended s and p carriers of ZnO. Thus, the carriers are spin-polarized and can mediate ferromagnetic ordering of the magnetic moments of TM ions doped into the oxide lattice, i.e., TM ions replace Zn^{2+} sites.[13] Defects and formation of secondary phases are supposed to play a crucial role in ferromagnetic ordering, which are introduced by the doping of transition metals in ZnO. Also, the magnetic properties, i.e., saturation magnetization M_s and coercivity H_c can be modified by dopant ions.[14,15] Along with the magnetic alterations, doping strongly affects the structural properties as well because the lattice parameters and unit cell volume vary by the addition of dopant ions.[16] Moreover, doping of ZnO with metallic elements results in an enhancement of its properties depending on the application field, such as silver (Ag) and aluminum (Al) for transparent conductive oxide (TCO), magnesium (Mg) for breath analysis devices, and manganese (Mn) for DMS or antibacterial thin films.[17] Many researchers work on zinc oxide semiconductors doped with Mg, Fe, Co, Ni, Al, or Li to achieve room-temperature ferromagnetism.[18−20]

Mn being a common metallic dopant of ZnO nanoparticles has been discussed in publications. Ma and Wang[21] observed particle size variation with calcination temperature and increased UV light absorption with decreasing particle size. Senthil Kumar et al. observed that increasing Mn concentration decreased ZnO nanopowder transmittance and particle size.[22] Some studies observed that ferromagnetism in Mn/ZnO nanoparticles referred to the existence of manganese oxides.[23,24] Mera et al.[25] demonstrated the room-temperature ferromagnetism behavior of ZnO doped with 0.02−0.1 mol of Mn^{+2} thin films synthesized by pulsed-laser deposition. Ilyas et al.[26] obtained ZnO doped with Mn by the centrifugation coating technique on the Si substrate, with Mn^{+2} concentrations ranging from 0.02 to 0.05 mol, indicating the formation of a single phase with ferromagnetism at room temperature. Torquato et al.[27] revealed the fact that the incorporation of Mn^{+2} ions in ZnO nanoparticles enhanced the magnetic properties, saturation magnetization, and Curie temperature in particular. Yan et al.[28] demonstrated that Zn vacancies favored RTFM in Mn-doped ZnO. It is evident that Mn-doped ZnO is among the most popular systems in the literature because of its high thermal solubility and high magnetic moments at room temperature. For improving the productivity of ZnO/Mn nanoparticles, these studies play a crucial role.

For the synthesis of TM-doped ZnO nanoparticles, a number of procedures have been developed, including the coprecipitation method, the autocombustion method, the ball milling method, and the solid-state reaction method.[29] Among all of the techniques, the sol−gel autocombustion method has certain primacy due to the following reasons: (i) easy control of shape and size of particles, (ii) the method is easy and without costly equipment, (iii) requires less time, and (iv) enables effective isolation as well as purification of the required products.[30] The product possesses better morphology owing to its fine particle size. Also, the magnetic behavior of TM-doped ZnO nanoparticles is sensitive to the synthesis method because the variation of particle size, product purity, good chemical homogeneity, and better crystallinity modifies the saturation magnetization and magnetic anisotropy, which is of immense importance for RTFM.[31] Therefore, we have selected the good-control and low-cost sol−gel method to form Mn-doped ZnO nanoparticles. This study looked into the impact of Mn doping on the structural, optical, and magnetic characteristics of ZnO nanoparticles.

RESULTS AND DISCUSSION

X-ray Diffraction. Figure 1a displays the XRD spectra of ZnO and $Zn_{1-x}Mn_xO$ (x = 0.01, 0.03, 0.04) nanoparticles. A hexagonal wurtzite structure with a high degree of crystallinity is assured by specific (1 0 0), (0 0 2), and (1 0 1) planes having diffraction peaks at 31.9, 34.5, and 36.6° of 2θ, respectively, which is similar to the standard data of pure ZnO

https://doi.org/10.1021/acsomega.3c03418
ACS Omega 2023, 8, 28749−28757

Table 1. Physical Characteristics of Pure and Mn-Doped ZnO Nanoparticles

contents	2θ (deg)	$a = b$ (Å)	c (Å)	$\frac{c}{a}$	FWHM (deg)	d-spacing (Å)	volume (Å)^3
ZnO	36.35	3.2472	5.2033	1.6024	0.3576	2.493	47.51
$Zn_{0.99}Mn_{0.01}O$	36.28	3.2491	5.2068	1.6025	0.4831	2.450	47.60
$Zn_{0.97}Mn_{0.03}O$	36.38	3.2501	5.2079	1.6024	0.5656	2.452	47.64
$Zn_{0.96}Mn_{0.04}O$	36.36	3.2516	5.2089	1.6020	0.6053	2.453	47.69

(a = 3.2488 Å, c = 5.2061 Å, space group $P63mc$, 186, matched with pdf data card No. 36-1451).[32] The XRD spectrum shows two to three broad peaks for each sample, proving that the nanoparticles are polycrystalline. Six major peaks indexed as (1 0 0), (0 0 2), (1 0 1), (1 0 2), (1 1 0), and (1 0 3) with diffraction intensity maximum at (1 0 1) lie from 35.6 to 37.2° for all of the samples.

Debye Scherer's equation determines the average crystal size.[32]

$$\text{average crystal size } (D) = 0.9\lambda/\beta \cos\theta \quad (1)$$

where θ is the Bragg's angle, β is the entire width at half-maximum of the (101) peak, and λ is the wavelength of the incident light, which is 1.45 Å.

The following relation calculates unit cell volume

$$V = 0.866a^2c \quad (2)$$

XRD results revealed that all of the prepared samples are polycrystalline having (1 0 1) prominent orientation along the c-axis. Compared with the pure ZnO sample, there are some weak intensity peaks for $Zn_{0.96}Mn_{0.04}O$, which are due to the $ZnMn_2O_4$ phase, which has a tetragonal structure. This is an indication that Mn^{2+} substitutes Zn without disturbing the wurtzite structure. As the Mn concentration increases, the intensity of (1 0 1) peaks of the samples becomes weaker, indicating a decline in crystallinity with more Mn incorporation. Small peak broadening occurs by increasing Mn concentration, which is due to the increased strain by Mn incorporation in the Zn lattice site.[33]

Table 1 shows the increasing values of FWHM and the volume of pure ZnO and Mn-doped ZnO nanoparticles. This indicates the fall off of crystal quality by increasing the Mn concentration in the nanoparticles. Indeed, the lattice parameters of a semiconductor depend on foreign atoms, defects, and the difference in ionic radii with respect to the substituted ions. Figure 1b shows that the reason for the slight shift of the (1 0 1) peak is probably the doping of Mn^{2+}, which has a relatively high ionic radius (0.080 nm), at places where Zn^{2+} ions have a smaller ionic radius (0.074 nm), expanding the lattice parameter and slightly increasing the a- and c-axis lattice constant.[34] The c/a ratio shows a negligible variation for all of the samples, showing no change in the hexagonal wurtzite structure of the host crystal by the incorporation of the dopant.

Figure 2 shows the variation of FWHM and crystallite size. By increasing Mn concentration in ZnO crystals, FWHM values increase from 0.3576° to 0.6053° and particle size dropped from 38.42 to 27.54 nm. The reason for this is the increase in lattice distortion and strain induced due to the substitution of Mn^{2+}, as the ionic radius of Mn^{2+} (0.080 nm) is larger than that of Zn^{2+} (0.074 nm). So, the disfigurement in ZnO lattice by Mn^{2+} decreases the nucleation and succeeding progress rate by increasing Mn concentration.[35]

The dislocation density (δ) and lattice strain (η) of the (1 0 1) peak was computed by using the following equations[36]

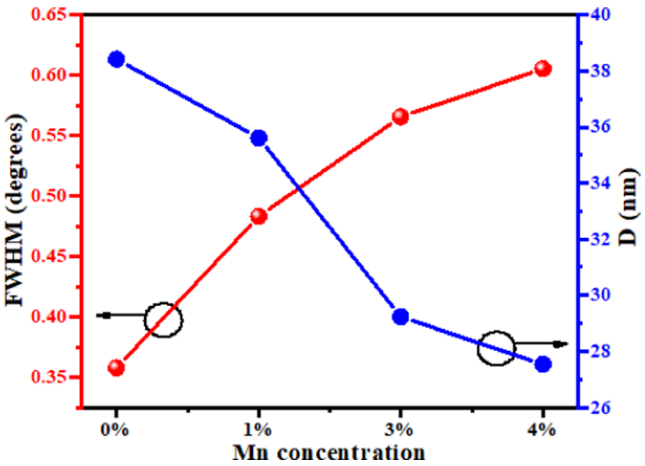

Figure 2. FWHM and crystallite size of pure ZnO and Mn-doped ZnO nanoparticles.

$$\delta = \frac{1}{D^2} \quad (3)$$

$$\eta = \frac{\beta \cos\theta}{4} \quad (4)$$

The width of the diffraction peak (1 0 1) broadens, which is also the evidence of an increase in lattice distortion and strain induced due to the substitution of Mn^{2+} that can be justified by the fact that the ionic radius of Mn^{2+} is larger than that of Zn^{2+}. The dislocation density increases from 0.0067712 to 0.013184 nm^{-2}, while the lattice strain increases from 0.006961 to 0.011865 as the doping concentration increases to 4%. The fluctuation of the (1 0 1) peak's average crystallite size, dislocation density (δ), and lattice strain (η) in all samples is shown in Table 2.

Table 2. Average Crystallite Size (D), Dislocation Density (δ), and Lattice Strain (η) of Pure ZnO and Mn-Doped ZnO Nanoparticles

sample	D (nm)	δ ($\times 10^{-3}$ nm^{-2})	η ($\times 10^{-2}$)
ZnO	38.42	6.7712	0.6961
$Zn_{0.99}Mn_{0.01}O$	35.61	7.8860	0.9162
$Zn_{0.97}Mn_{0.03}O$	29.23	11.704	1.1174
$Zn_{0.96}Mn_{0.04}O$	27.54	13.184	1.1865

Surface Morphology. The surface morphology of ZnO and Mn-doped ZnO nanoparticles is examined using scanning electron microscopy (SEM). The SEM image of ZnO nanoparticles in Figure 3a has a blend of spherical and hexagonal-like structures. Cluster-shaped random agglomeration with the dominant hexagonal structure was observed for all of the doped samples (Figure 3b–d). The average crystallite size decreases gradually by increasing dopant concentration. The grain size of pure ZnO is ~34 nm and that of doped

https://doi.org/10.1021/acsomega.3c03418
ACS Omega 2023, 8, 28749−28757

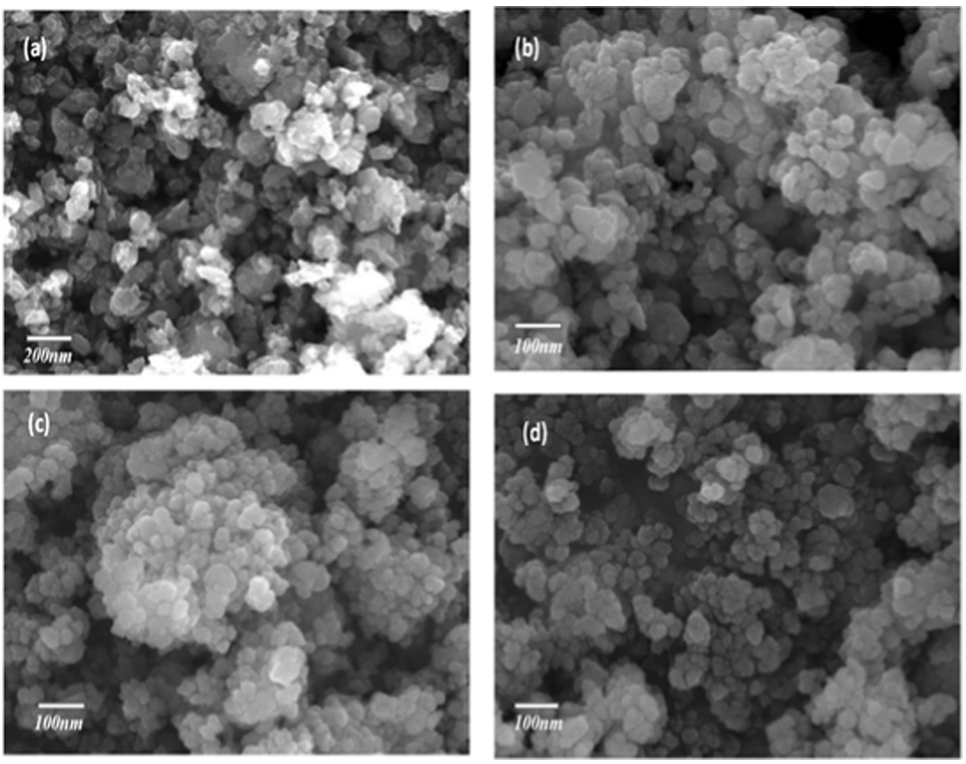

Figure 3. SEM micrographs of (a) pure ZnO, (b) $Zn_{0.99}Mn_{0.01}O$, (c) $Zn_{0.97}Mn_{0.03}O$, and (d) $Zn_{0.96}Mn_{0.04}O$ nanoparticles.

samples is around ∼25 nm.[37] All SEM images reveal fine compatibility with the XRD patterns.

OPTICAL PROPERTIES

Figure 4 shows the reflectance spectra of ZnO, $Zn_{0.99}Mn_{0.01}O$, $Zn_{0.97}Mn_{0.03}O$, and $Zn_{0.96}Mn_{0.04}O$ nanoparticles by UV−vis diffuse reflectance spectroscopy (DRS) in the wavelength range from 300 to 800 nm. For a sample of pure ZnO, the absorption edge is about 460 nm and is shifted to about 670 nm by the Mn dopant.[38] Maximum reflectance (∼82%) is noticed for ZnO nanoparticles, which considerably reduces to around 40% by doping Mn.

Optical absorption spectra at room temperature were obtained in the wavelength range of 200−1200 nm, as shown in Figure 5. Absorption mainly relies on the band gap, oxygen deficiency, impurities, and texture of the surface.

According to Senthilkumaar et al., all absorption curves show intense absorption in the 200−370 nm wavelength range, with the absorption edge being between 290 and 350 nm due to the high exciton binding energy.[39] The optical band gap was computed using the Tauc relation[39]

$$(\alpha h\nu)^2 = A(h\nu - E_g) \quad (5)$$

where A is a constant, $h\nu$ is the photon energy, and E_g represents the energy band gap. Figure 6 shows the Tauc plot and the variation of the energy band gap by increasing dopant concentration.

The band gap for the pure ZnO sample is found to be 3.25 eV and it decreases to 3.02 eV by the addition of Mn. By increasing Mn concentration to 4%, the band gap further reduces to 2.62 eV. The absorption edge has been shifted to lower energies. It is believed that both the defect states and disorder produced by increasing doping concentration can be a reason for band tails and the narrowing of the band gap. Studies have also shown that the reduction in ZnO's energy band gap is predominantly caused by the sp−d spin−exchange interaction between band electrons and the localized spin of transition metal ions. The conduction and valence band energies are corrected negatively and positively, respectively, by the s−d and p−d exchange interactions, which causes a narrowing of the band gap.[40] Here, the band gap reduces from 3.25 eV for undoped ZnO nanoparticles to 2.62 eV for $Zn_{0.96}Mn_{0.04}O$; the red shift in the band gap is attributed to this spin−exchange interaction. These results are in line with the literature results. Table 3 shows the calculated band gap values for all of the samples.

FOURIER TRANSFORM INFRARED SPECTROSCOPY

The band locations and relative absorption peaks depend on chemical and morphological configurations. Figure 7 shows the FTIR spectra from 4000 to 400 cm^{-1} of ZnO, $Zn_{0.99}Mn_{0.01}O$, $Zn_{0.97}Mn_{0.03}O$, and $Zn_{0.96}Mn_{0.04}O$ nanoparticles. Infrared peak modes and assignments are shown in Table 4.

The absorption peaks around 3525 cm^{-1} are associated with the polymeric O—H stretching vibration of a small amount of H_2O in ZnO nanocrystals, which may result from moisture in the atmosphere. Here, these vibrations are present in very minute magnitude, which suggests less surface defects. Consequently, the concentration of surface defects can be indirectly inferred from the intensities of vibrations of hydroxyl groups. Weak bands around 2340 cm^{-1} due to the C−H stretching mode were also recorded. Peaks of O═C═O stretching can be seen at 1982 and 1984 cm^{-1} for pure ZnO and 4% Mn-doped ZnO nanoparticles, respectively, while it was observed at 1404 and 1314 cm^{-1} previously. The H−O−H bending vibration around 1620 cm^{-1} is missing in our case. Some weak bands around 865, 884, and 866 cm^{-1} in the doped

https://doi.org/10.1021/acsomega.3c03418
ACS Omega 2023, 8, 28749−28757

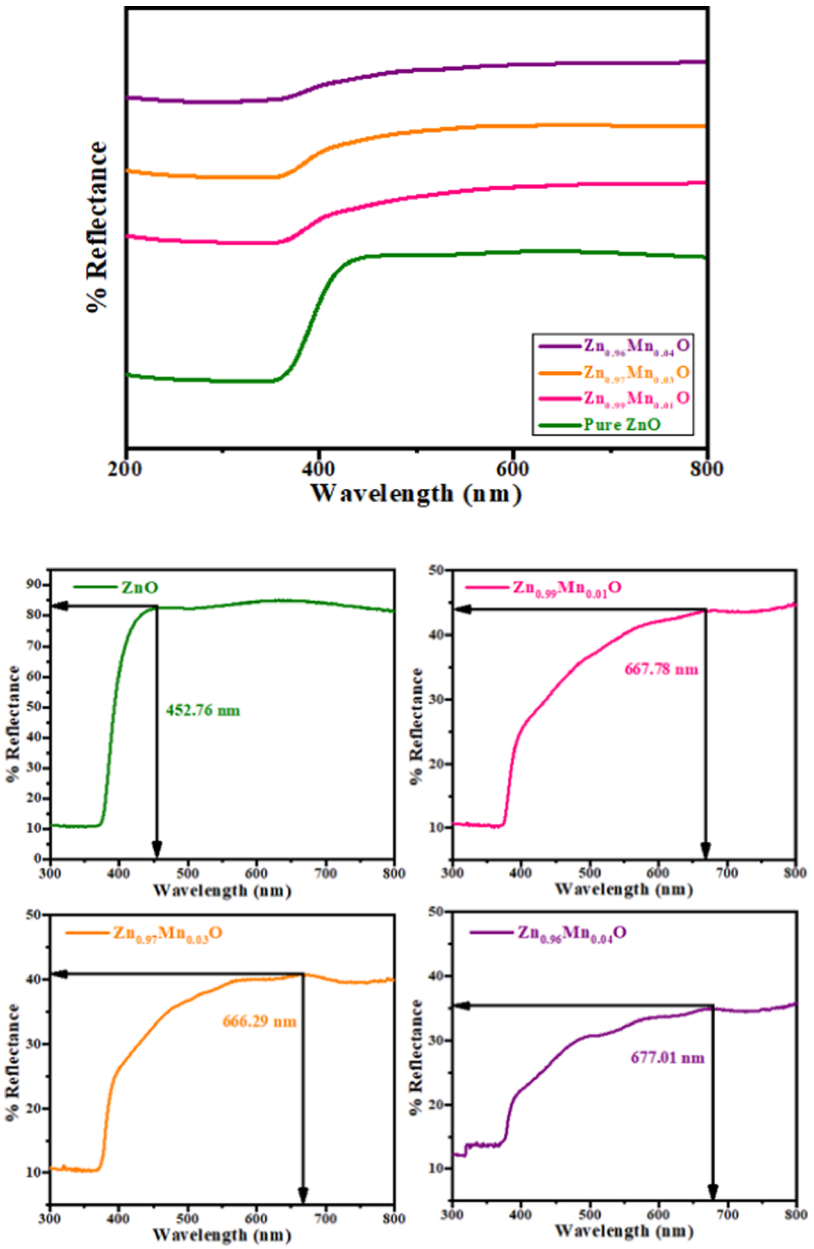

Figure 4. Reflectance spectra of pure ZnO and Mn-doped ZnO nanoparticles.

spectra appeared due to a microstructural vibrational feature of Mn doping.[41] The minor variation in their intensities by varying Mn concentrations is because of the density of defect states surrounding dopant ions in the ZnO lattice. The absorption band observed in undoped ZnO at 516.57 cm^{-1} is due to Zn−O stretching; this band was shifted to 512 cm^{-1} with a slight decrease when Mn doping was increased. The slight shift in the position of the absorption band by increasing the Mn concentration is because of incorporation of Mn^{2+} ions in the ZnO lattice.[42]

Vibrating Sample Magnetometer (Magnetic Properties). DMS's magnetic properties mostly depend on the synthesis method, the dopant, and the annealing temperature. The M−H loop is shown in Figure 8, and its findings proved that pure ZnO is diamagnetic at room temperature.[43]

Figure 9 shows that the Mn-doped ZnO samples exhibit ferromagnetic behavior at low concentrations, and for higher concentrations, they show both paramagnetic and ferromagnetic behaviors.[44] Table 5 shows that saturation magnetization varies from 0.013 to 0.035 emu/g as the Mn concentration increases from 1 to 4%. Sharma et al. reported the same results for similar concentrations.[45] If we probe the reason for observed room-temperature ferromagnetic behavior in Mn-doped ZnO samples, there are several mechanisms that are responsible for this. It can be induced due to the lattice distortions and defects caused by the incorporation of the Mn dopant into the ZnO lattice due to the difference in their ionic radii. Another reason for room-temperature ferromagnetism could be the presence of secondary phases.[46] In our work, XRD studies did not show any evidence of secondary phases, so the observed ferromagnetism can be the intrinsic property of Mn-doped ZnO samples.

Another mechanism that contributes to RTFM in Mn-doped ZnO nanoparticles is the ferromagnetic coupling of the local moment of Mn dopants via the sp−d exchange interaction. To mediate the long-range ferromagnetic order, the Mn moments

https://doi.org/10.1021/acsomega.3c03418
ACS Omega 2023, 8, 28749−28757

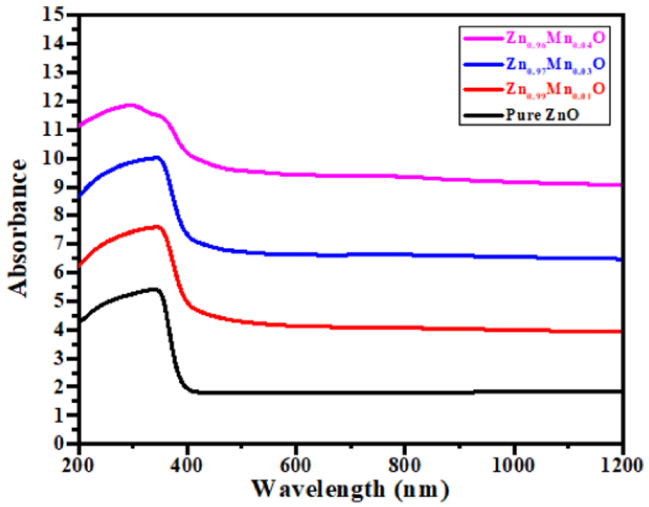

Figure 5. Absorbance spectra of pure ZnO and Mn-doped ZnO nanoparticles.

must couple together. In our situation, a strong sp−d exchange interaction between the band electrons of ZnO and the localized d electrons of Mn ions substituting for Zn^{+2} ions has already been explained as the cause of the reduction in the optical band gap. So, this might be a more dominant reason contributing to the observed RTFM in Mn-doped ZnO nanoparticles in our study. A similar interpretation was considered by Shatnawi et al.[47]

Table 3. Values of Energy Band Gaps for All of the Samples

sample	E_g (eV)
ZnO	3.25
$Zn_{0.99}Mn_{0.01}O$	3.02
$Zn_{0.97}Mn_{0.03}O$	3.16
$Zn_{0.96}Mn_{0.04}O$	2.62

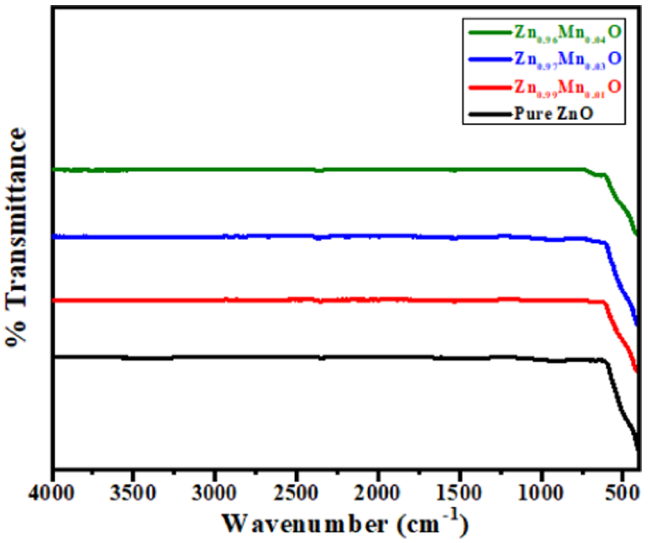

Figure 7. FTIR spectra from 4000−400 cm^{-1} of pure ZnO and Mn-doped ZnO nanoparticles.

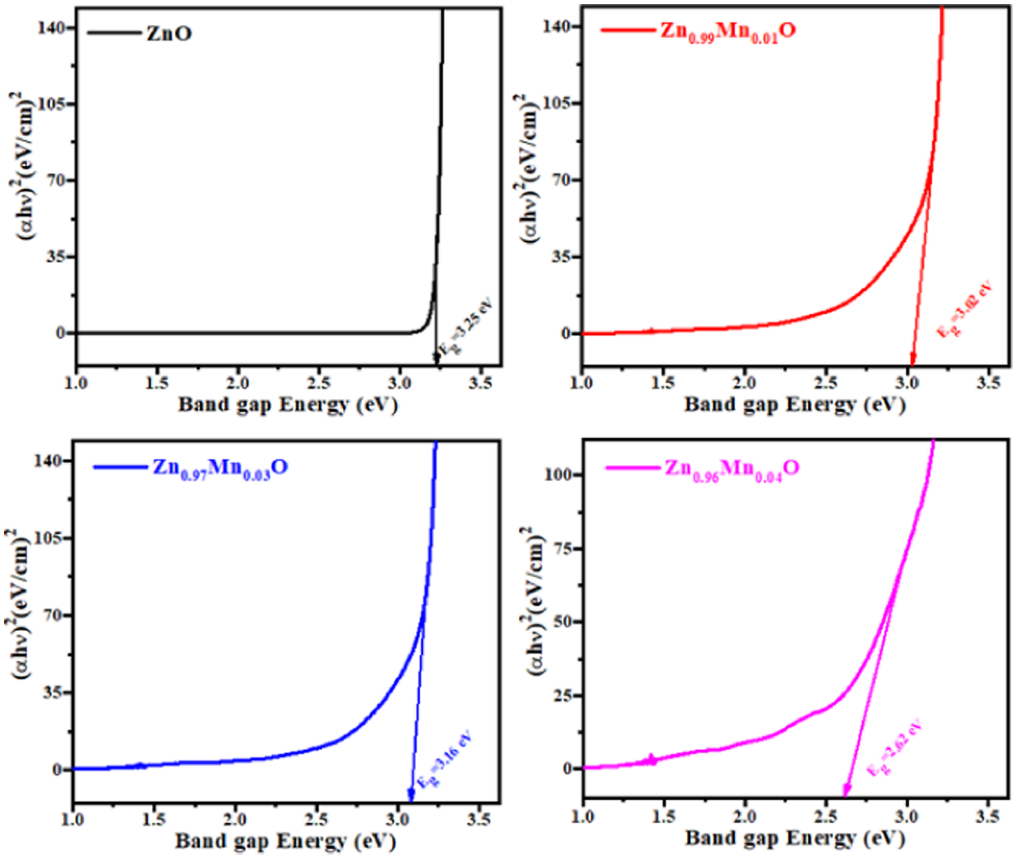

Figure 6. Tauc plot of pure ZnO and Mn-doped ZnO nanoparticles.

https://doi.org/10.1021/acsomega.3c03418
ACS Omega 2023, 8, 28749−28757

Table 4. IR Transmission Peaks and Their Assignments of Pure ZnO and Mn-Doped ZnO Nanoparticles

	wavenumber (cm^{-1})			
assignments	pure ZnO	$Zn_{0.99}Mn_{0.01}O$	$Zn_{0.97}Mn_{0.03}O$	$Zn_{0.96}Mn_{0.04}O$
O−H stretching	3647.82	3648	3647.38	3525.65
weak C−H bending	2340.67	2339.40	2340.96	2341
stretching O═C═O	1982	1981.86	1985.4	1984.07
vibrational mode of Zn−Mn−O	absent	865.76	884.87	866.5
stretching Zn−O	516	512	509	511

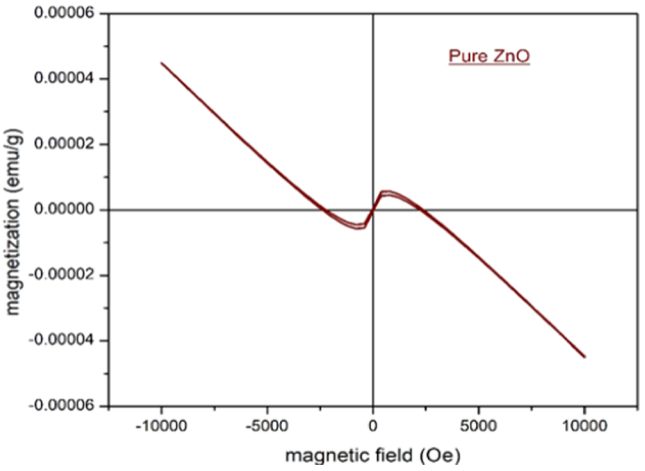

Figure 8. Pure ZnO magnetometer results for a vibrating sample.

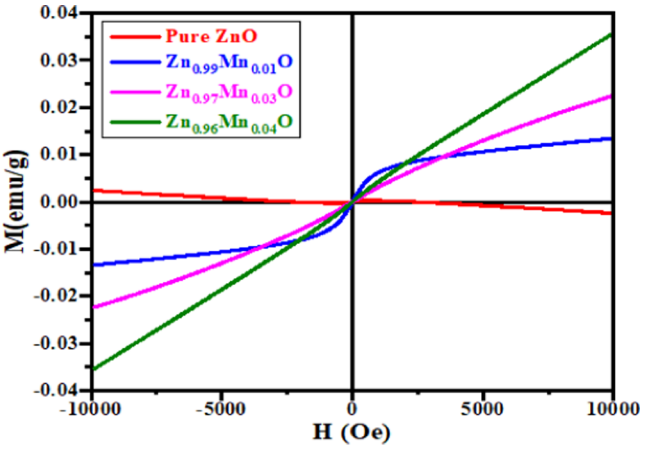

Figure 9. Results of the VSM of pure ZnO and Mn-doped ZnO nanoparticles.

CONCLUSIONS

The sol−gel autocombustion method was employed to synthesize pure ZnO and Mn-doped ZnO nanoparticles. The average crystallite size was reduced from 38.42 to 27.54 nm by increasing the dopant concentration. Dislocation density and lattice strain increased for doped samples compared to those for pure ZnO, indicating that the Mn^{2+} ions are well integrated into the ZnO lattice. SEM images show the spherical and hexagon homogeneous-like shapes, which seconds the XRD data for the average grain size. UV−vis diffuse reflectance spectroscopy showed the maximum reflectance for pure ZnO. UV−visible absorption measurements and FTIR spectroscopy confirm the successful incorporation of Mn ions into the ZnO lattice. In the VSM study, the doped samples displayed room-temperature ferromagnetism. Doping of Mn increases the saturation magnetization of the sample. The observed RTFM in doped nanoparticles is mostly generated by the sp−d exchange interaction of ZnO band electrons and Mn localized d electrons. This is also the reason for the decrease in the energy band gap from 3.25 to 2.99 eV. This work is helpful for fabricating transition metal-doped ZnO nanoparticles with improved optical and magnetic characteristics for numerous of spintronics applications.

EXPERIMENTAL DETAILS

Materials. All of the starting raw materials, including $[Zn(NO_3)_2.6H_2O]$ (Ag−99%, Sigma−Aldrich), $[Mn(NO_3)_2.4H_2O]$ (Ag−99%, Sigma−Aldrich), sodium hydroxide, ethylene glycol, citric acid, and ammonia, were used as received without extra refining. All of the chemicals were of analytical grade.

Synthesis. ZnO and $Zn_{(1-x)}$ Mn_x O (x = 0.01, 0.03, 0.04) nanoparticles were synthesized by using the sol−gel method. First, the required amount of water (312 mL) was taken in a beaker, which was put on a hot plate. Then, the required amount of $[Zn(NO_3)_2{\cdot}6H_2O]$ was added to the beaker and stirred. After stirring for 25 min, we added the required amount of $[Mn(NO_3)_2{\cdot}4H_2O]$ in the beaker, followed by constant stirring for 20 min more to get better results. After stirring for few seconds, the required amounts of citric acid and ethylene glycol were added as a catalyst. To maintain the pH between 9 and 10, some amount of ammonia was added. After maintaining the pH, the temperature was adjusted to 80 °C for 2 h.

After 2 h, the temperature was raised to 120 °C and the solution was changed to a gel form. After some time, the gel started burning, which assured that the sample was synthesized successfully. Then, the sample was dried in an oven at 80 °C for 2 h. After drying, the sample was ground to change it into fine powder. After that, the sample was annealed at 300 °C for 3 h in a box furnace under air. After annealing, the samples were ready for different characterization techniques.

Table 5. Saturation Magnetization and Retentivity of the Samples with Mn Doping

samples	saturation magnetization (emu/g)	coercivity (Oe)	remnant magnetization (emu/g)
$Zn_{0.99}Mn_{0.01}O$	0.013	15.16	1.42
$Zn_{0.97}Mn_{0.03}O$	0.022	28.52	1.05
$Zn_{0.96}Mn_{0.04}O$	0.035	8.53	3.98

https://doi.org/10.1021/acsomega.3c03418
ACS Omega 2023, 8, 28749−28757

CHARACTERIZATION TECHNIQUES

The structural characteristics and phase analysis of pure and Mn-doped ZnO were examined by X-ray diffraction (XRD) with Cu Kα radiations (λ = 1.54 Å) at 40 kV and 30 mA for 2θ = 20−80°. The surface morphology was determined by scanning electron microscopy (SEM). Fourier transform infrared (FTIR) spectroscopy was evaluated to analyze the infrared (IR) spectra of absorption and reflection in the 1800−200 cm^{-1} range. Ultraviolet−visible (UV−vis) spectroscopy was employed to study optical behavior. The magnetic properties (M−H curves) were assessed using a vibrating sample magnetometer (VSM) at room temperature with an applied field of 10 kOe.

AUTHOR INFORMATION

Corresponding Authors

Muhammad Tahir Khan − *Department of Physics, Riphah International University, Islamabad 44000, Pakistan*; Email: tahir_iiui14@yahoo.com

Abid Zaman − *Department of Physics, Riphah International University, Islamabad 44000, Pakistan*; orcid.org/0000-0001-9527-479X; Email: zaman.abid87@gmail.com

Authors

Sidra Kanwal − *Department of Physics, Riphah International University, Islamabad 44000, Pakistan*

Vineet Tirth − *Mechanical Engineering Department, College of Engineering, King Khalid University, Abha 61421 Asir, Kingdom of Saudi Arabia; Research Center for Advanced Materials Science (RCAMS), King Khalid University, Abha 61413 Asir, Kingdom of Saudi Arabia*; orcid.org/0000-0002-8208-7183

Ali Algahtani − *Mechanical Engineering Department, College of Engineering, King Khalid University, Abha 61421 Asir, Kingdom of Saudi Arabia; Research Center for Advanced Materials Science (RCAMS), King Khalid University, Abha 61413 Asir, Kingdom of Saudi Arabia*

Tawfiq Al-Mughanam − *Department of Mechanical Engineering, College of Engineering, King Faisal University, Al-Ahsa 31982, Kingdom of Saudi Arabia*

Complete contact information is available at: https://pubs.acs.org/10.1021/acsomega.3c03418

Notes

The authors declare no competing financial interest.

ACKNOWLEDGMENTS

The authors extend their appreciation to the Deanship of Scientific Research at King Khalid University Abha 61421, Asir, Kingdom of Saudi Arabia for funding this work through the General Groups Project under grant number RGP.2/499/44. The authors acknowledge the Deanship of Scientific Research, Vice Presidency for Graduate Studies and Scientific Research at King Faisal University, Saudi Arabia, for financial support under the annual funding track [GRANT3820].

REFERENCES

(1) Daniel, M. C.; Astruc, D. Gold nanoparticles: assembly, supramolecular Chemistry, quantum-size-related properties, and applications toward biology, catalysis and nanotechnology. *Chem. Rev.* **2004**, *104*, 293−346.

(2) Faivre, D.; Bennet, M. Magnetic nanoparticles line up. *Nature* **2016**, *535*, 235−236.

(3) Yu, H.; Chen, Y.; Wei, W.; Ji, X.; Chen, L. A Functional Organic Zinc-Chelate Formation with Nanoscaled Granular Structure Enabling Long-Term and Dendrite-Free Zn Anodes. *ACS Nano* **2022**, *16*, 9736−9747.

(4) Reiss, G.; Hütten, A. Applications beyond data storage. *Nat. Mater.* **2005**, *4*, 725−726.

(5) Pan, P.; Chen, X.; Xing, H.; Deng, Y.; Chen, J.; Alharthi, F. A.; Alghamdi, A. A.; Su, J. A fast on-demand preparation of injectable self-healing nanocomposite hydrogels for efficient osteoinduction. *Chin. Chem. Lett.* **2021**, *32*, 2159−2163.

(6) Djurišić, A.; Ng, A. M. C.; Chen, X. Y. ZnO nanostructures for optoelectronics: Material properties and device applications. *Prog. Quantum Electron.* **2010**, *34*, 191−259.

(7) Devillers, T.; Jamet, M.; Barski, A.; Poydenot, V.; Dujardin, R.; Bayle Guillemaud, P.; Tatarenko, S. Structural and magnetic properties of GeMn layers; High Curie temperature ferromagnetism induced by selforganized GeMn nano-columns. *Phys. Status Solidi (a)* **2007**, *204*, 130−135.

(8) Yang, Z. A perspective of recent progress in ZnO diluted magnetic semiconductors. *Appl. Phys. A* **2013**, *112*, 241−254.

(9) Banu Bahşi, Z.; Oral, A. Y. Effects of Mn and Cu doping on the microstructures and optical properties of sol−gel derived ZnO thin films. *Opt. Mater.* **2007**, *29*, 672−678.

(10) Zhang, Z.; Yi, J. B.; Ding, J.; Wong, L. M.; Seng, H. L.; Wang, S. J.; Wu, T.; et al. Cu-doped ZnO nanoneedles and nanonails: morphological evolution and physical properties. *J. Phys. Chem. C* **2008**, *112*, 9579−9585.

(11) Dietl, T.; Ohno, O. H.; Matsukura, A. F.; Cibert, J.; Ferrand, E. D. Zener model description of ferromagnetism in zinc-blende magnetic semiconductors. *Science* **2000**, *287*, 1019−1022.

(12) Torquato, R. A.; Shirsath, S. E.; Kiminami, R. H. G. A.; Costa, A. C. F. M. Synthesis and structural, magnetic characterization of nanocrystalline Zn1− xMnxO diluted magnetic semiconductors (DMSs) synthesized by combustion reaction. *Ceram. Int.* **2014**, *40*, 6553−6559.

(13) Bhatti, K. P.; Kundu, S.; Chaudhary, S.; Kashyap, S. C.; Pandya, D. K. Observation of room temperature ferromagnetism in nano-crystalline ZnO: Co system. *J. Phys. D: Appl. Phys.* **2006**, *39*, 4909.

(14) Patange, S. M.; Desai, S. S.; Meena, S. S.; Yusuf, S. M.; Shirsath, S. E. Random site occupancy induced disordered Néel-type collinear spin alignment in heterovalent Zn^{2+}−Ti^{4+} ion substituted $CoFe_2O_4$. *RSC Adv.* **2015**, *5*, 91482−91492.

(15) Tomboc, G. M.; Zhang, X.; Choi, S.; Kim, D.; Lee, L. Y. S.; Lee, K. Stabilization, Characterization, and Electrochemical Applications of High-Entropy Oxides: Critical Assessment of Crystal Phase−Properties Relationship. *Adv. Funct. Mater.* **2022**, *32*, No. 2270242.

(16) Mane, D. R.; Birajdar, D. D.; Shirsath, S. E.; Telugu, R. A.; Kadam, R. H. Structural and magnetic characterizations of Mn−Ni−Zn ferrite nanoparticles. *Phys. Status Solidi (a)* **2010**, *207*, 2355−2363.

(17) Wang, M.; Zhang, T.; Cui, M.; Liu, W.; Liu, X.; Zhao, J.; Zhou, J. Sub-nanopores-containing N, O-codoped porous carbon from molecular-scale networked polymer hydrogel for solid-state supercapacitor. *Chin. Chem. Lett.* **2021**, *32*, 1111−1116.

(18) Haque, M. J.; Bellah, M. M.; Hassan, M. R.; Rahman, S. Synthesis of ZnO nanoparticles by two different methods & comparison of their structural, antibacterial, photocatalytic and optical properties. *Nano Express* **2020**, *1*, No. 010007.

(19) Darvishi, E.; Kahrizi, D.; Arkan, E. Comparison of different properties of zinc oxide nanoparticles synthesized by the green (using Juglans regia L. leaf extract) and chemical methods. *J. Mol. Liq.* **2019**, *286*, No. 110831.

(20) Wu, X.; Wei, Z.; Zhang, L.; Wang, X.; Yang, H.; Jiang, J. Optical and magnetic properties of Fe doped ZnO nanoparticles obtained by hydrothermal synthesis. *J. Nanomater.* **2014**, *2014*, 1−6.

(21) Nakayama, M.; Tanaka, H.; Masuko, K.; Fukushima, T.; Ashida, A.; Fujimura, N. Photoluminescence properties peculiar to the Mn-related transition in a lightly alloyed ZnMnO thin film grown by pulsed laser deposition. *Appl. Phys. Lett.* **2006**, *88*, No. 241908.

(22) Philipose, U.; Nair, S. V.; Trudel, S.; De Souza, C. F.; Aouba, S.; Hill, R. H.; Ruda, H. E. High-temperature ferromagnetism in Mn-doped ZnO nanowires. *Appl. Phys. Lett.* **2006**, *88*, No. 263101.
(23) Deka, S.; Joy, P. A. Synthesis and magnetic properties of Mn doped ZnO nanowires. *Solid State Commun.* **2007**, *142*, 190−194.
(24) Yang, H. Y.; Lee, S. H.; Kim, T. W. Effect of zinc nitrate concentration on the structural and the optical properties of ZnO nanostructures. *Appl. Surf. Sci.* **2010**, *256*, 6117−6120.
(25) Mera, J.; Córdoba, C.; Doria, J.; Paucar, C.; Gómez, A.; Fuchs, D.; Morán, O. Distinct magnetic response of nanograined Zn1−xMnxO (x = 0, 0.02, 0.1) powders and thin films: Focus on the effect of the working atmosphere. *Vacuum* **2012**, *86*, 1605−1612.
(26) Ilyas, U.; Rawat, R. S.; Wang, Y.; Tan, T. L.; Lee, P.; Chen, R.; Zhang, S.; et al. Alteration of Mn exchange coupling by oxygen interstitials in ZnO: Mn thin films. *Appl. Surf. Sci.* **2012**, *258*, 6373−6378.
(27) Torquato, R. A.; Shirsath, S. E.; Kiminami, R. H. G. A.; Costa, A. C. F. M. Synthesis and structural, magnetic characterization of nanocrystalline Zn1-xCoxO diluted magnetic semiconductors (DMS) synthesized by combustion reaction. *Ceram. Int.* **2018**, *44*, 4126−4131.
(28) Yan, W.; Sun, Z.; Liu, Q.; Li, Z.; Pan, Z.; Wang, J.; Zhang, X.; et al. Zn vacancy induced room-temperature ferromagnetism in Mn-doped ZnO. *Appl. Phys. Lett.* **2007**, *91*, No. 062113.
(29) Dinesha, M. L.; Jayanna, H. S.; Mohanty, S.; Ravi, S. Structural, electrical and magnetic properties of Co and Fe co-doped ZnO nanoparticles prepared by solution combustion method. *J. Alloys Compd.* **2010**, *490*, 618−623.
(30) Shirsath, S. E.; Wang, D.; Jadhav, S. S.; Mane, M. L.; Li, S. Ferrites obtained by sol-gel method. *Handb. Sol-Gel Sci. Technol.* **2018**, 695−735.
(31) Klein, L.; Aparicio, M.; Jitianu, A. (Eds.). *Handbook of Sol-Gel Science and Technology, Processing, Characterization and Applications*, Springer: Cham, 2016, pp 695−735.
(32) Zaman, A.; Uddin, S.; Mehboob, N.; Ali, A. Structural investigation and improvement of microwave dielectric properties in Ca (HfxTi1-x) O3 ceramics. *Phys. Scr.* **2020**, *96*, No. 025701.
(33) El Mir, L.; Amlouk, A.; Barthou, C.; Alaya, S. Synthesis and luminescence properties of ZnO/Zn2SiO4/SiO2 composite based on nanosized zinc oxide-confined silica aerogels. *Phys. B: Cond. Matt.* **2007**, *388*, 412−417.
(34) Anghel, J.; Thurber, A.; Tenne, D. A.; Hanna, C. B.; Punnoose, A. Correlation between saturation magnetization, bandgap, and lattice volume of transition metal (M = Cr, Mn, Fe, Co, or Ni) doped Zn 1−x M x O nanoparticles. *J. Appl. Phys.* **2010**, *107*, No. 09E314.
(35) Ashokkumar, M.; Muthukumaran, S. Microstructure and band gap tailoring of Zn0. 96− xCu0. 04CoxO (0 ⩽ x ⩽ 0.04) nanoparticles prepared by co-precipitation method. *J. Alloys Compd.* **2014**, *587*, 606−612.
(36) Ali, A.; Zaman, A.; Aldulmani, S. A.; Abbas, M.; Mushtaq, M.; Bashir, K.; Amami, M.; Althubeiti, K. Structural Evolution and Microwave Dielectric Properties of Ba1−x Sr x Ti4O9,(0.0 ≤ *x* ≤ 0.06) Ceramics. *ACS Omega* **2022**, *7*, 2331−2336.
(37) El Ghoul, J.; Barthou, C.; Saadoun, M.; El Mir, L. Synthesis and optical characterization of SiO2/Zn2SiO4: Mn nanocomposite. *Phys. B: Cond. Matt.* **2010**, *405*, 597−601.
(38) Senol, S. D.; Yalcin, B.; Ozugurlu, E.; Arda, L. Structure, microstructure, optical and photocatalytic properties of Mn-doped ZnO nanoparticles. *Mater. Res. Express* **2020**, *7*, No. 015079.
(39) Senthilkumaar, S.; Rajendran, K.; Banerjee, S.; Chini, T. K.; Sengodan, V. Influence of Mn doping on the microstructure and optical property of ZnO. *Mater. Sci. Semicond. Process.* **2008**, *11*, 6−12.
(40) El-Hilo, M.; Dakhel, A. A. Structural and magnetic properties of Mn-doped ZnO powders. *J. Magn. Magn. Mater.* **2011**, *323*, 2202−2205.
(41) Husain, S.; Alkhtaby, L. A.; Giorgetti, E.; Zoppi, A.; Miranda, M. M. Effect of Mn doping on structural and optical properties of sol gel derived ZnO nanoparticles. *J. Lumin.* **2014**, *145*, 132−137.
(42) Guo, Y.; Cao, X.; Lan, X.; Zhao, C.; Xue, X.; Song, Y. Solution-based doping of manganese into colloidal ZnO nanorods. *J. Phys. Chem. C* **2008**, *112*, 8832−8838.
(43) Potzger, K.; Zhou, S.; Eichhorn, F.; Helm, M.; Skorupa, W.; Mücklich, A.; Bianchi, A.; et al. Ferromagnetic Gd-implanted ZnO single crystals. *Appl. Phys. Lett.* **2006**, *99*, No. 063906.
(44) Kanwal, S.; Khan, M. T.; Mehboob, N.; Amami, M.; Zaman, A. Room-temperature ferromagnetism in Cu/Co Co-doped ZnO nanoparticles prepared by the co-precipitation method: for spintronics applications. *ACS Omega* **2022**, *7*, 32184−32193.
(45) Sharma, P.; Gupta, A.; Rao, K. V.; Owens, F. J.; Sharma, R.; Ahuja, R.; Gehring, G. A.; et al. Ferromagnetism above room temperature in bulk and transparent thin films of Mn-doped ZnO. *Nat. Mater.* **2003**, *2*, 673−677.
(46) Li, J. H.; Shen, D. Z.; Zhang, J. Y.; Zhao, D. X.; Li, B. S.; Lu, Y. M.; Liu, Y.; Fan, X. W. Magnetism origin of Mn-doped ZnO nanoclusters. *J. Magn. Magn. Mater.* **2006**, *302*, 118−121.
(47) Shatnawi, M.; Alsmadi, A. M.; Bsoul, I.; Salameh, B.; Mathai, M.; Alnawashi, G.; Bawa'aneh, M. S.; et al. Influence of Mn doping on the magnetic and optical properties of ZnO nanocrystalline particles. *Results Phys.* **2016**, *6*, 1064−1071.

https://doi.org/10.1021/acsomega.3c03418
ACS Omega 2023, 8, 28749−28757